Applied Catalysis B: Environmental 333 (2023) 122771

Contents lists available at ScienceDirect

Applied Catalysis B: Environmental

journal homepage: www.elsevier.com/locate/apcatb

Distinctive *p-d* orbital hybridization in RuSb nanobranches for simultaneously enhanced hydrogen evolution and hydrazine oxidation in alkaline seawater

Xiaofei Liu [a,*], Tianxing Wang [a], Yilin Chen [a], Jingtao Wang [a], Wenjie Xie [b], Rongqian Wu [a,c], Xingtao Xu [d], Lihui Pang [c], Xiaogang Zhang [e], Yi Lv [a,c], Guangzhao Wang [b,*], Yusuke Yamauchi [d,f,g,**], Tian (Leo) Jin [h,*]

[a] Center for Regenerative and Reconstructive Medicine, Med-X Institute, The First Affiliated Hospital of Xi'an Jiaotong University, Xi'an, Shaanxi Province, China
[b] Key Laboratory of Extraordinary Bond Engineering and Advanced Materials Technology of Chongqing, School of Electronic Information Engineering, Yangtze Normal University, Chongqing 408100, China
[c] National Local Joint Engineering Research Center for Precision Surgery & Regenerative Medicine, Shaanxi Provincial Center for Regenerative Medicine and Surgical Engineering, The First Affiliated Hospital of Xi'an Jiaotong University, Xi'an, Shaanxi Province, China
[d] International Center for Materials Nanoarchitectonics (WPI–MANA), National Institute for Materials Science (NIMS), Tsukuba, Ibaraki 305-0044, Japan
[e] Department of Hepatobiliary Surgery, The First Affiliated Hospital of Xi'an Jiaotong University, Xi'an, Shaanxi Province, China
[f] School of Chemical Engineering and Australian Institute for Bioengineering and Nanotechnology (AIBN), The University of Queensland, Brisbane, Queensland 4072, Australia
[g] Department of Materials Science and Engineering, School of Engineering, Nagoya University, Furo-cho, Chikusa-ku, Nagoya 464-8601, Japan
[h] Department of Applied Chemistry, School of Chemistry, MOE Key Laboratory for Nonequilibrium Synthesis and Modulation of Condensed Matter (Xi'an Jiaotong University) Xi'an Key Laboratory of Sustainable Energy Materials Chemistry, State Key Laboratory of Electrical Insulation and Power Equipment, State Key Laboratory for Mechanical Behavior of Materials, Xi'an Jiaotong University, Xi'an, Shaanxi Province, China

ARTICLE INFO

Keywords:
p-d hybridization
Nanobranch
Hydrogen evolution
Hydrazine oxidation
Alkaline seawater

ABSTRACT

Orbital hybridization is a powerful tool for modulating electronic structures toward various electrocatalytic reactions. Compared to the widely reported *d-d* hybridization in *d*-block metal alloys, the *p-d* orbital hybridization between *d*-block metals and *p*-block elements could provide new opportunities for regulating the electronic properties and thus promoting the electrocatalytic activities. Herein, we report a distinctive *p*-block metalloid-regulating *p-d* orbital hybridization to realize the fabrication of RuSb nanobranches for bifunctional hydrogen evolution (HER) and hydrazine oxidation (HzOR), which exhibits huge potential in overall hydrazine splitting (OHzS) by utilizing thermodynamically favorable HzOR instead of sluggish oxygen evolution on the anode. To our delight, RuSb delivers an impressively low overpotential of 39 mV for HER and 252 mV for HzOR at 10 mA cm^{-2} in alkaline seawater. The two-electrode OHzS electrolyzer with RuSb||RuSb couple can achieve outstanding electrocatalytic activity with an extraordinarily small cell voltage of 35 mV to drive 10 mA cm^{-2} in alkaline seawater, outperforming the Pt/C||Pt/C couple under the same condition. Density functional theory calculations further indicate that the Sb doping can not only mediate the adsorption energy for hydrogen but also the energy barrier for the dehydrogenation of $*N_2H_3$. Therefore, our work verifies the huge potential of *p-d* orbital hybridization for the development of a bifunctional OHzS system in alkaline seawater.

1. Introduction

Hydrogen production has been widely recognized as a sustainable and efficient alternative to fossil fuels owing to its highest energy density and zero-emission [1]. The electrocatalytic hydrogen evolution reaction (HER), a cathode reaction during water-splitting, has aroused extensive

* Corresponding authors.
** Corresponding author at: International Center for Materials Nanoarchitectonics (WPI–MANA), National Institute for Materials Science (NIMS), Tsukuba, Ibaraki 305-0044, Japan
E-mail addresses: xiaofeiliu@xjtu.edu.cn (X. Liu), wangyan6930@126.com (G. Wang), y.yamauchi@uq.edu.au (Y. Yamauchi), tianjin.ecust@gmail.com (T.(L. Jin).

https://doi.org/10.1016/j.apcatb.2023.122771
Received 17 February 2023; Received in revised form 25 March 2023; Accepted 13 April 2023
Available online 21 April 2023
0926-3373/

research interest so far [2–7]. This process has the advantage of being sustainable and pollution-free, especially when the electrical energy is obtained from wind and solar [8–12]. However, the intrinsically sluggish kinetics of anodic oxygen evolution reaction (OER) during water-splitting is considered as the bottleneck due to the high energy consumption of the four-electron-transfer process. Recently, overall hydrazine splitting (OHzS) has emerged as a new alternative to conventional water splitting, utilizing anodic hydrazine oxidation reaction (HzOR) to replace OER at a much lower cell voltage [13–15]. Despite some progress that has been achieved, several key challenges remain as it is at the infant stage [16–18]. First, the working potential is still far beyond the thermodynamic value and thus the overpotential is still unsatisfactory. Second, the development of bifunctional electrocatalysts toward both HER and HzOR mechanisms with low cost is still challenging, raising demanding requirements on smart designing strategies. Third, the strict requirement of high-purity water as the electrolyte restricts the large deployment of this technology. To this end, exploring highly efficient and low-cost bifunctional HER and HzOR electrocatalysts, especially utilizing almost infinite seawater as the electrolyte is of vital importance.

Currently, noble metal platinum (Pt)-based composites with low overpotential have been widely explored. However, the scarcity and high cost of Pt pose huge challenges for the practical application of the electrochemical water-splitting process [19–24]. To this end, other economical non-Pt electrocatalysts with Pt-like performance show great potential in HER. Up to now, ruthenium (Ru)-based electrocatalysts have emerged as an encouraging alternative due to their high intrinsic activity, exhibiting comparable Pt-like activity due to similar interaction with hydrogen compared with Pt (~65 kcal mol^{-1}) [25–28]. However, the price of metallic Ru (42 $ per oz) is only ~ 4% of metallic Pt (992 $ per oz), providing more opportunities for HER catalysts [29–31]. More importantly, Ru sites could also stabilize the HzOR intermediates and decrease the energy barrier for HzOR [32–34]. As such, intensive studies have been carried out on various Ru-based electrocatalysts such as Ru single atoms, Ru nanoclusters, and Ru-based alloys [35–38]. Among them, Ru-based alloys sparked our great interest as the hybridization of multiple metal sites could significantly boost the intrinsic activity due to the electronic coupling between multiple *d*-block metal sites and therefore, optimized H adsorption. For example, bimetal Ru-based alloys such as RuFe [39], RuCo [40], RuNi [41], RuPt [42], and RuPd [43] have been widely investigated to enhance hydrogen production. The introduction of these new *d*-orbital electrons may dramatically rebuild the electronic configuration around Ru sites via optimized *d-d* interaction [25]. Nevertheless, *p*-block metals or metalloids, which possess a nature of metallicity or dual nature of metallicity/non-metallicity, have rarely been explored for electrocatalysis. Not only the difficulty of synthetic strategy to fabricate such Ru-based alloys but also closed *d* shells (d^{10} electron configuration) of these *p*-block elements hinder the *d-d* interaction and therefore limit the potential application in electrocatalysis. Interestingly, several pioneering works indicate that these *p*-block elements may also be promising for catalysis through careful engineering [44–46]. As such, the unique *p*-block metal/metalloid regulation of Ru sites beyond conventional *d-d* interaction could provide new opportunity for the OHzS system, with both improved HER and HzOR performance.

With these considerations in mind, herein, we established a synthetic strategy for fabricating *p*-block metalloid (Sb)-regulating RuSb nanobranches featuring an unconventional *p-d* orbital hybridization interaction. Surprisingly, the introduction of Sb not only can regulate the Ru active center for HER but also mediate the energy barrier for the HzOR. Owing to the well-optimized electronic coupling between Ru and Sb, the as-synthesized catalyst exhibits excellent bifunctional performance for both HER and HzOR in alkaline seawater. To our delight, RuSb delivers an impressively low overpotential of 39 mV with Pt-like activity at 10 mA cm^{-2} in alkaline seawater. Meanwhile, RuSb also exhibits remarkable performance for HzOR, with a low overpotential of 252 mV at 10 mA cm^{-2}. Therefore, the RuSb||RuSb couple in the overall hydrazine splitting system exhibits remarkable electrocatalytic activity with an extraordinarily small cell voltage of 35 mV to drive 10 mA cm^{-2} in alkaline seawater, outperforming the Pt/C||Pt/C couple under the same condition. Density functional theory (DFT) calculations further indicate that the Sb doping can not only make the hydrogen adsorption more thermoneutral but also decrease the energy barrier for dehydrogenation from $*N_2H_3$ to $*N_2H_2$. Therefore, the strategy of regulating both HER and HzOR performance via *p-d* orbital hybridization provides new opportunities for the development of the OHzS system.

2. Experimental section

2.1. Chemicals

All commercially were used without further purification. Ruthenium (III) acetylacetonate (98%) was purchased from Shanghai Yien Chemical Technology Co., Ltd. Antimony trichloride (99%) was obtained from Adamas Reagent, Ltd. Polyvinylpyrrolidone (molecular weight≈58000) was obtained from Macklin. Ammonium bromide (99%) was purchased from Aladdin.

2.2. Synthesis of RuSb and Ru

In a typical synthesis, ruthenium (III) acetylacetonate (100 mg), antimony trichloride (40 mg), polyvinylpyrrolidone (1 g), and ammonium bromide (120 mg) were mixed in benzyl alcohol (100 mL) and heated at 200 °C for 4 h. The obtained solid was washed with ethanol and acetone before drying. The molar ratio between Ru and Sb was determined to be 1.04:1 by inductively coupled plasma-optical emission spectrometry (ICP-OES), indicating the equimolar of Ru and Sb in RuSb. Therefore, the obtained sample was denoted as $Ru_{50}Sb_{50}$. Ru was synthesized following a similar method without adding antimony trichloride. Another two Ru_xSb_{1-x} samples with different Ru contents ($Ru_{62}Sb_{38}$ and $Ru_{36}Sb_{64}$) were synthesized based on a similar method by using 20 mg of antimony trichloride and 50 mg of ruthenium (III) acetylacetonate, respectively.

2.3. Material characterization

Powder X-ray diffraction (XRD) measurements were carried out on a Bruker D8 ADVANCE diffractometer. High-resolution transmission electron microscopy (HRTEM) was performed on JEM-F200. Scanning electron microscopy (SEM, Gemini SEM 500) was utilized to determine the morphology of the samples. X-ray photoelectron spectroscopy (XPS) was determined by Thermo Fisher ESCALAB Xi+ spectrometer. The chemical composition was determined by ICP-OES on NexION 350D. Nitrogen sorption at 77 K was obtained on the NOVA touch 4LX gas sorption analyzer.

2.4. Electrochemical test

The electrocatalytic HER and HzOR were carried out on a CHI 760E electrochemical workstation. 1 M KOH and 0.5 M H_2SO_4 solution were used as the electrolyte for HER, respectively. 1 M KOH + 0.5 M N_2H_4 was used as the electrolyte for HzOR. A glassy carbon (GC) and a graphite rod were utilized as the working electrode and the counter electrode, respectively. A Hg/HgO and a Hg/Hg_2SO_4 electrode were used as the reference electrode in alkaline and acid electrolytes, respectively. The determined potential was converted to the reversible hydrogen electrode (RHE). To obtain the working electrode, 5 mg of the catalyst was mixed with 50 μL of Nafion D-520 dispersion and sonicated 950 μL of ethanol for at least 30 mins. Subsequently, the catalyst ink (20 μL) was drop-dried onto a GC electrode and dried at ambient conditions (catalyst loading: ~0.51 mg cm^{-2}). During the HER test, the electrolyte was bubbled with high-purity Ar. The scan rate of linear scan voltammetry

(LSV) was 2 mV s^{-1}. 95% iR-compensation was made to compensate for the voltage drop. The mass activity (mA mg^{-1}) was calculated from the Ru loading (*m*) and the measured current density (*j*) by the formula of mass activity= *j/m*. The electrochemical active surface area (ECSA) was evaluated by the double-layer capacitance (C_{dl}) following the formula of ECSA=C_{dl}/C_s. The C_{dl} can be calculated by cyclic voltammetry with various scan rates (20, 40, 60, 80 and 100 mV s^{-1}). The C_{dl} was obtained based on the slope of the linear fit. The C_s is the average value of specific capacitance, which is estimated to be 40 μF cm^{-2} in alkaline media.[47, 48] The electrochemical impedance spectra (EIS) measurements were performed in 1 M KOH (HER) or 1 M KOH + 0.5 M N_2H_4 (HzOR) from 10^{-2}-10^5 Hz with an AC voltage amplitude of 10 mV. For overall hydrazine splitting, the catalyst was loaded on carbon paper (Toray) and used as both anode and cathode in 1 M KOH + 0.5 M N_2H_4. The seawater was collected from the Yellow Sea (Rizhao, China) and filtered before use. To keep the concentration of hydrazine during the stability test, the fresh electrolyte was added continuously by a peristaltic pump. The quantity of generated H_2 and N_2 was collected by a drainage method with colored water for clarity.

3. Results and discussion

3.1. Material preparation and characterizations

As illustrated in Fig. 1a, we successfully synthesized both RuSb alloy ($Ru_{50}Sb_{50}$) and Ru by a facile hydrothermal method (synthesis details can be found in the experimental section). The composition and structure were then investigated and shown in Fig. 1 a-j. To illustrate the structure features of obtained samples, the XRD pattern was first carried out to determine the crystallinity (Fig. 1b). Ru displays six representative peaks at 38.3°, 42.1°, 44.0°, 58.3°, 69.4°, and 78.4°, which is a typical hexagonal phase of Ru (JCPDS No. 70–0274). Interestingly, RuSb exhibits a broad peak at ~42°, indicating a poor crystallinity. The morphology of RuSb and Ru was then determined by scanning electron microscopy (SEM, Fig. S1), which indicates both granulated-like morphology of our samples. To further confirm the structural characteristic of RuSb, HRTEM (Fig. 1c-d) was utilized. According to statistical analysis (Fig. S2), uniform dispersion of RuSb nanobranches can be observed, with an average diameter of 5.6 nm. Moreover, the HRTEM image of RuSb further reveals the crystalline nature as evidenced by randomly oriented lattice fringes (Fig. 1f). In addition, an in-depth

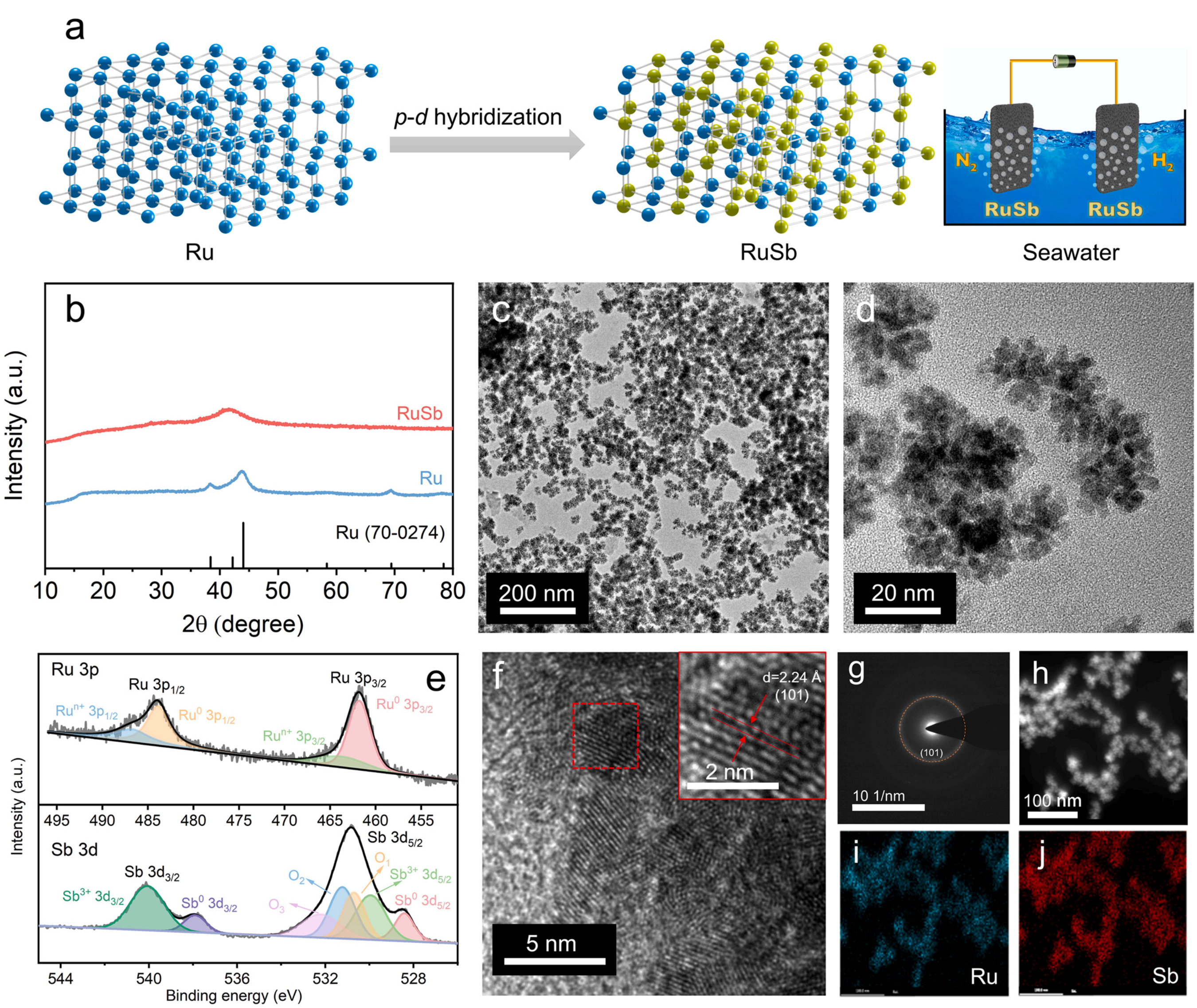

Fig. 1. (a) Simplified description of the strategy used in this work. (b) XRD patterns of RuSb, Ru, and the typical Ru phase (JCPDS No. 70–0274). (c-d) TEM images of RuSb. (e) XPS spectra of Ru 3p and Sb 3d regions of RuSb. (f) HRTEM lattice fringe image of RuSb. (g) The FFT pattern extracted from the HRTEM image. (h-j) EDX elemental mapping of Ru and Sb in RuSb.

analysis of the selected area for RuSb reveals the *d*-spacing of 2.24 Å, corresponding to the (101) plane of hexagonal Ru (Fig. 1g and S3-S4). In contrast, pristine Ru exhibits a slightly decreased *d*-spacing of 2.08 Å. The *d*-spacing of RuSb is larger than that of pristine Ru, due to the expansion of the lattice after introducing larger Sb atoms (Fig. S5). The corresponding mapping images reveal that Ru and Sb are uniformly distributed in RuSb (Fig. 1h-j). From the N_2 adsorption/desorption isotherms at 77 K, after introducing Sb, the BET surface area is slightly increased up to 9.4 m^2 g^{-1} (Fig. S6).

To probe the chemical state of the RuSb surface, XPS was carried out. As revealed in the Ru 3*p* spectrum in Fig. 1e, the peaks at 461.8 and 484.0 eV could be attributed to Ru^0 $3p_{3/2}$ and Ru^0 $3p_{1/2}$, while the other two peaks located at 463.7 and 485.8 eV may be ascribed to Ru^{n+} $3p_{3/2}$ and Ru^{n+} $3p_{1/2}$, respectively [37,49]. For comparison, we also determined the Ru valence in Ru. As illustrated in Fig. S7, the binding energy of metallic Ru is slightly higher than that in RuSb and the relative content of high-valence Ru increased in metallic Ru, which is a clear evidence of electron transfer from Sb to Ru [50,51]. Moreover, for the Sb 3*d* spectrum, two typical peaks at binding energies of 528.4 and 537.9 eV are attributed to Sb^0 $3d_{5/2}$ and Sb^0 $3d_{3/2}$, respectively. Meanwhile, the peaks at 529.9 and 540.1 are assigned to Sb^{3+} $3d_{5/2}$ and Sb^{3+} $3d_{3/2}$, respectively. The existence of a positive oxidation state of Sb

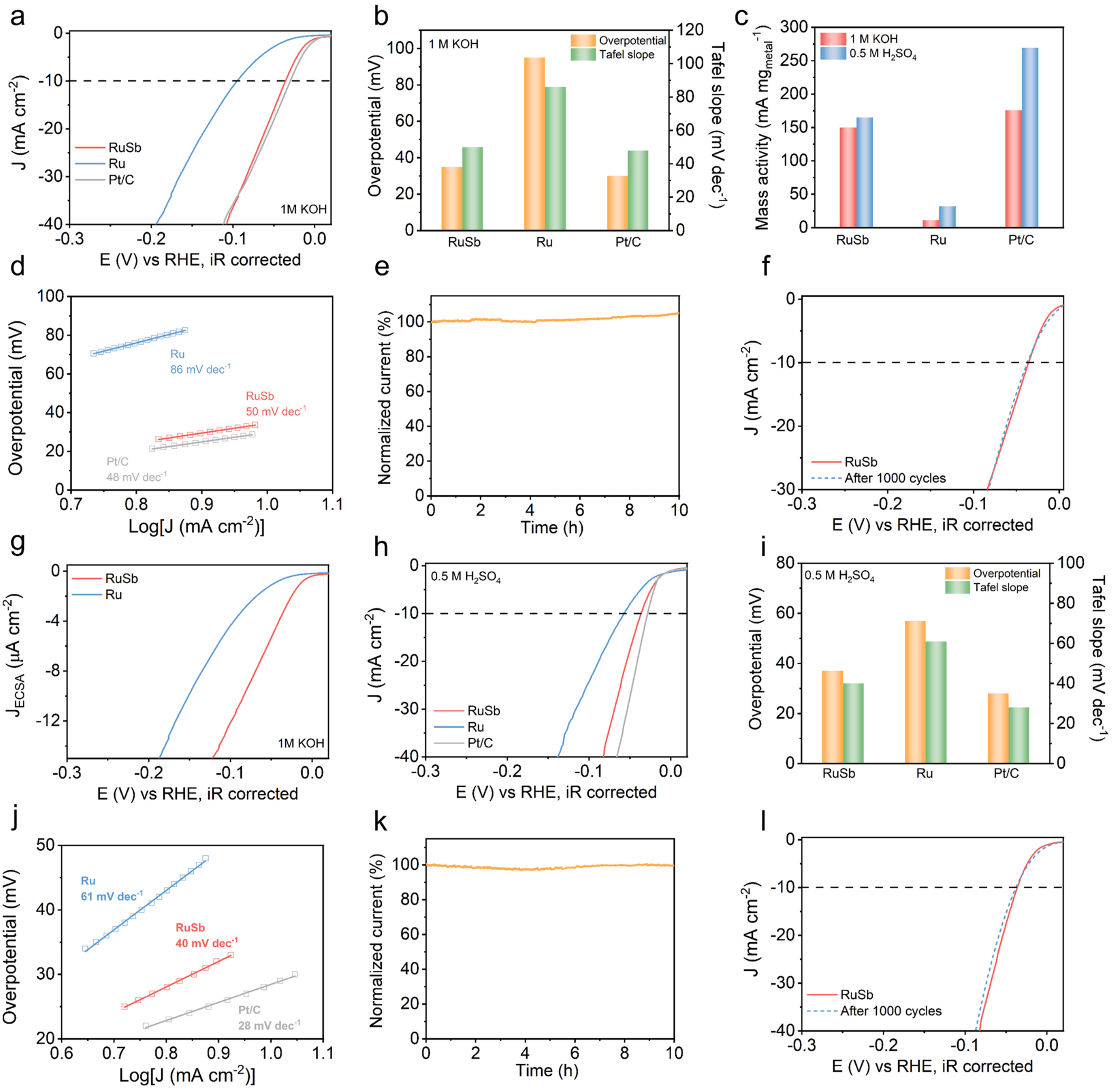

Fig. 2. (a) HER polarization curves of the RuSb, Ru, and 20% Pt/C in 1 M KOH, respectively. (b) Comparison of overpotential and Tafel slope for HER on the obtained catalysts in 1 M KOH. (c) The mass activity of the catalyst in both 1 M KOH and 0.5 M H_2SO_4. (d) The Tafel plots of the obtained catalysts in 1 M KOH. (e) Chronoamperometric test of the RuSb for HER in 1 M KOH at − 0.05 V. (f) LSV of the RuSb before and after 1000 continuous CV cycles in 1 M KOH. (g) LSV curves for HER normalized by ECSA on RuSb and Ru in 1 M KOH, respectively. (h) HER polarization curves of the RuSb, Ru, and 20% Pt/C in 0.5 M H_2SO_4, respectively. (i) Comparison of overpotential and Tafel slope on the obtained catalysts in 0.5 M H_2SO_4. (j) The Tafel plots of the obtained catalysts in 0.5 M H_2SO_4. (k) Chronoamperometric test of the RuSb in 0.5 M H_2SO_4 at − 0.05 V. (l) LSV of the RuSb before and after 1000 continuous CV cycles in 0.5 M H_2SO_4.

reveals that Sb loses electrons and transfers to Ru, which is consistent with the Ru 3*p* spectrum. In addition, the O 1*s* peaks located at 530.7, 531.3, and 532.2 can also be observed, which is the typical signal for lattice oxygen, defective/hydroxyl group, and adsorbed water, respectively. These results confirm the successful formation of RuSb alloy and pure Ru phase by our synthetic method.

3.2. Exploring the HER performance

As a proof of concept, the effect of *p*-block metalloid on HER performance was first investigated on a GC electrode in Ar-saturated 1 M KOH utilizing a standard three-electrode configuration. A Hg/HgO electrode and a graphite rod work as the reference and counter electrodes, respectively (details can be found in the characterization section). As illustrated in Fig. 2a-b, RuSb exhibits an impressive low overpotential of 35 mV @ 10 mA cm^{-2} in 1 M KOH, indicating Pt-like activity compared with the benchmark 20% Pt/C (30 mV @ 10 mA cm^{-2}). In contrast, Ru only displays a large overpotential of 95 mV @ 10 mA cm^{-2}. Furthermore, the mass activity of RuSb at an overpotential of 50 mV is calculated to be 150 mA mg^{-1} by normalizing to the Ru loading (Fig. 2c), which is 13.6 times higher than Ru (11 mA mg^{-1}) and very close to the 20% Pt/C (176 mA mg^{-1}). Furthermore, pure Sb shows no activity towards HER under the same condition (Fig. S8). Therefore, we can confirm that the *p*-block metalloid (Sb) optimized the electronic structure and could significantly improve the HER performance. It should be mentioned that this RuSb outperformed many state-of-the-art Ru-based HER electrocatalysts and a comprehensive comparison can be found in Table S1.

To better understand the HER kinetics, the corresponding Tafel plots of RuSb, Ru, and 20% Pt/C were also plotted (Fig. 2d). As such, the Tafel slope of RuSb was calculated to be 50 mV $decade^{-1}$, which is very close to 20% Pt/C (48 mV $decade^{-1}$). Compared with Ru (86 mV $decade^{-1}$), fast kinetics was observed for RuSb, revealing that the hydrogen generation on RuSb proceeds through the Volmer-Heyrovsky mechanism. As such, the rate-determining step (RDS) for this process should be electrochemical desorption [52]. Furthermore, the electrochemical HER stability of RuSb was evaluated by a chronoamperometric test. As illustrated in Fig. 2e, the current-time curve only shows a slight loss at the beginning and reaches almost stable after 4 h. We also performed the stability test at a larger current density on carbon paper around 58 mA cm^{-2}, with ~7.2% current loss after 10 h (Fig. S9). The accelerated stability test by cycling the RuSb for continuous 1000 CV cycles showed nearly no difference from the initial one (Fig. 2f), further confirming its robust stability in 1 M KOH. In addition, the ECSA was further measured by the C_{dl}. As a result, the ECSA was calculated to be 588 and 498 cm^2 for RuSb and Ru, respectively (Fig. S10 and S11). Therefore, a normalized LSV plot can further confirm the better catalytic activity of RuSb over Ru (Fig. 2g). Additionally, EIS was also carried out to investigate the charge transport for HER (Fig. S12a,b). As shown in Fig. S12a, RuSb exhibits a much smaller semicircle compared to Ru, indicating its lower charge transfer barrier, and thereby promoting the HER process. To further present the intrinsic activity of the catalysts, turnover frequency (TOF) was also calculated (details can be found in the supporting information). As illustrated in Fig. S13, the Sb-doping RuSb exhibits 9 times higher TOF (0.18 H_2 s^{-1}) compared with that in Ru (0.02 H_2 s^{-1}) at − 0.1 V (RHE) in 1 M KOH. Therefore, all these results reveal that *p*-block metalloid Sb can significantly boost the HER activity.

To evaluate the HER activity in a wide pH range of electrolytes, the performance of RuSb in 0.5 M H_2SO_4 was also investigated. As depicted in Fig. 2h-i, RuSb requires an overpotential of 37 mV to achieve 10 mA cm^{-2} in 0.5 M H_2SO_4, much higher than Ru (57 mV @ 10 mA cm^{-2}) comparable to commercial Pt/C (28 mV @ 10 mA cm^{-2}). Additionally, as illustrated in Fig. 2c, the mass activity of RuSb (165 mA mg^{-1}) is determined to be 5.2 times higher than Ru (32 mA mg^{-1}) and comparable to commercial Pt/C (269 mA mg^{-1}). Furthermore, the Tafel slope was confirmed as 40, 61, and 28 mV dec^{-1} for RuSb, Ru, and 20% Pt/C, respectively (Fig. 2i-j). Furthermore, similar stability experiments confirmed that no obvious current density loss of RuSb after 12 h of chronoamperometric test and continuous 1000 CV cycles (Fig. 2k and 2l). In addition, we also investigated the HER performance of RuSb in the neutral electrolyte. As shown in Fig. S14 and S15, RuSb also demonstrated competitive HER activity in the neutral PBS electrolyte, exhibiting a low overpotential of 65 mV @ 10 mA cm^{-2} and a Tafel slope of 160 mV dec^{-1}. Therefore, all these results confirm that RuSb displays excellent HER performance in a wide range of pH.

The effect of different Sb doping on HER performance was also investigated by optimizing the Ru/Sb ratio during the synthesis (details can be found in the experimental section). As a result, two new RuSb electrocatalysts ($Ru_{62}Sb_{38}$ and $Ru_{36}Sb_{64}$) with a Ru:Sb molar ratio of 1.6:1 and 0.57:1 were obtained, which can be confirmed by ICP. As illustrated in Fig. S16, a similar XRD pattern for both $Ru_{62}Sb_{38}$ and $Ru_{36}Sb_{64}$ compared with RuSb was obtained. Further HRTEM images indicate that both $Ru_{62}Sb_{38}$ and $Ru_{36}Sb_{64}$ display nanobranches morphology and increased *d*-spacing compared with Ru, which is consistent with the result of $Ru_{50}Sb_{50}$ (Fig. S17 and S18). Therefore, the HER performance was further determined in both alkaline and acidic electrolyte (Fig. S19 and S20). As a result, a slightly higher overpotential of 56 mV and 63 mV compared with the result of $Ru_{50}Sb_{50}$ was obtained for $Ru_{62}Sb_{38}$ and $Ru_{36}Sb_{64}$ at 10 mA cm^{-2} in 1 M KOH (Fig. S21a). Meanwhile, similar results were also observed in 0.5 M H_2SO_4 with an overpotential of 48 mV and 50 mV for $Ru_{62}Sb_{38}$ and $Ru_{36}Sb_{64}$, respectively. The corresponding mass activity of $Ru_{62}Sb_{38}$ and $Ru_{36}Sb_{64}$ further indicate that $Ru_{50}Sb_{50}$ exhibits the best HER activity in both alkaline and acidic electrolyte (Fig. S21b).

3.3. Exploring the HzOR performance

Inspired by the outstanding HER performance of RuSb, we further explore the electrocatalytic activity of RuSb towards HzOR. As illustrated in Fig. 3a, RuSb exhibits a remarkably low overpotential of 244 mV at 10 mA cm^{-2}, which is significantly lower than Ru (286 mV), 20% Pt/C (420 mV), and other previously reported catalysts (Table S2). The corresponding Tafel plot of RuSb is as low as 40.6 mV dec^{-1}, which is much lower than that of Ru (75.7 mV dec^{-1}) and Pt/C (57.7 mV dec^{-1}, Fig. 3b-c). Moreover, the long-term stability is further evaluated by the chronoamperometric measurement. As illustrated in Fig. 3d, where 96.4% current retention can be observed. In addition, ~6.1% current loss for HzOR was observed at ~52 mA cm^{-2} after 10 h of the chronoamperometric test (Fig. S22). Given both the excellent HER and HzOR activity of RuSb, we further investigate its performance in alkaline seawater. As displayed in Fig. 3e-f, a similar low overpotential of 39 mV for HER and 252 mV for HzOR at 10 mA cm^{-2} in alkaline seawater was obtained, indicating excellent adaptability of RuSb in alkaline seawater. The Tafel slope for HER and HzOR was also calculated to be 46 and 42.1 mV dec^{-1}, respectively, further revealing good kinetics of RuSb in alkaline seawater (Fig. S23a-b). EIS results further confirm the fast kinetics of RuSb over Ru for HzOR (Fig. S12b). Considering the remarkable performance of both HER and HzOR in the alkaline sweater, a two-electrode OHzS system was assembled in alkaline seawater using the RuSb as both the anode and cathode (Fig. S24). Impressively, the RuSb||RuSb couple exhibits outstanding electrocatalytic activity with a small cell voltage of 28 and 35 mV to drive 10 mA cm^{-2} in alkaline water and alkaline seawater, respectively, outperforming the Pt/C||Pt/C couple and most of the state-of-the-art electrocatalysts (Fig. 3g and Table S3). Fig. 3h further shows the LSV curves of RuSb||RuSb for OHzS and OWS systems in alkaline seawater. Obviously, compared with the OWS system, the OHzS system only requires a much smaller cell voltage to drive the same current density. Therefore, such an OHzS system with RuSb||RuSb couple can also be driven by a commercial AAA battery with 1.5 V voltage (Fig. 3i). Additionally, long-term stability measurement over

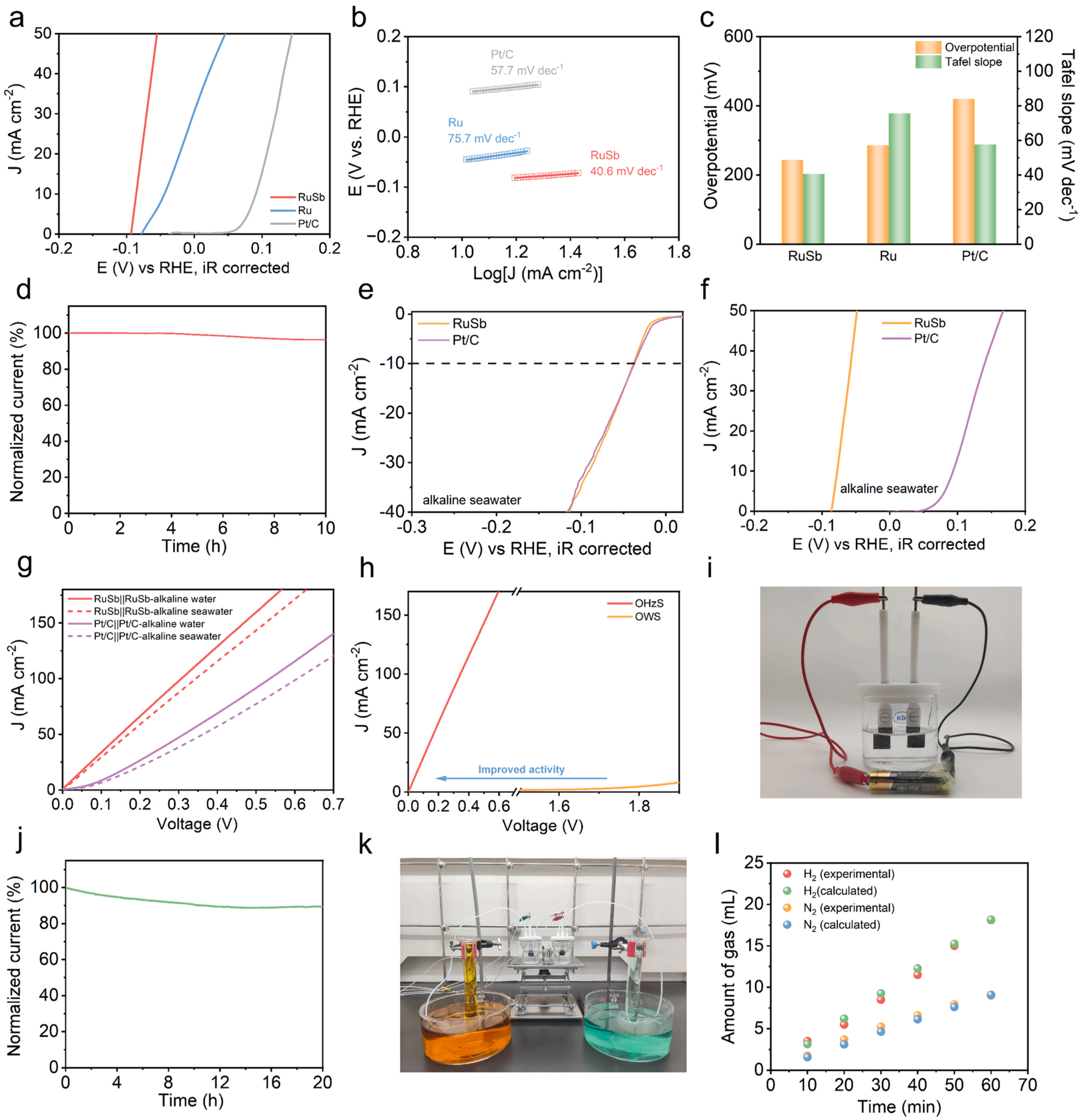

Fig. 3. (a) HzOR polarization curves of the RuSb, Ru, and 20% Pt/C in 1 M KOH+ 0.5 M N_2H_4, respectively. (b) The corresponding Tafel plots of the obtained catalysts for HzOR in 1 M KOH+ 0.5 M N_2H_4. (c) Comparison of overpotential and Tafel slope for HzOR on the obtained catalysts in 1 M KOH+ 0.5 M N_2H_4. (d) Chronoamperometric test of the RuSb in 1 M KOH+ 0.5 M N_2H_4 at − 0.08 V. (e) HER polarization curves of the RuSb and 20% Pt/C in 1 M KOH seawater, respectively. (f) HzOR polarization curves of the RuSb and 20% Pt/C in 1 M KOH+ 0.5 M N_2H_4 seawater, respectively. (g) Two-electrode electrolysis curves using RuSb||RuSb and Pt/C||Pt/C as bifunctional electrodes in 1 M KOH+ 0.5 M N_2H_4 and 1 M KOH+ 0.5 M N_2H_4 seawater, respectively. (h) LSV curves of OHzS and OWS for bifunctional RuSb||RuSb in 1 M KOH+ 0.5 M N_2H_4 seawater, respectively. (i) Optical image of an OHzS system with RuSb||RuSb couple driven by a 1.5 V AAA battery in alkaline seawater. (j) Durability tests of two-electrode electrolysis in 1 M KOH+ 0.5 M N_2H_4 seawater. (k) Optical image of homemade gas collection setup for the determination of H_2 and N_2 by a drainage method. (l) The generation rate of H_2 and N_2 in 1 M KOH+ 0.5 M N_2H_4 seawater at room temperature.

20 h reveals that over 89.3% of current density remains after continuous electrolysis in alkaline seawater (Fig. 3j). The morphological information of RuSb after stability tests was determined by SEM. As shown in Fig. S25, aggregated granular morphology can be confirmed after both HER and HzOR measurements. However, the similar XRD pattern of RuSb before and after the long-term stability test in alkaline seawater further confirmed the robustness of our catalysts (Fig. S26). Besides, a homemade gas collection setup for the determination of H_2 and N_2 was established based on a drainage method (Fig. 3k). As shown in Fig. 3l, the generation rate of H_2 and N_2 in alkaline seawater is close to 2:1 during the two-electrode electrolysis process, revealing nearly 100% Faradic efficiency in the OHzS system. These results demonstrate that

our RuSb could have great potential in implementing practical hydrogen production by feeding costless seawater and hydrazine near the coastal region.

3.4. DFT calculations

We further carried out calculations to obtain molecular-level insights into the excellent electrocatalytic HER and HzOR performance for RuSb. The RuSb and Ru surface models were first established and shown in Fig. 4a and b. Furthermore, the density of states (DOS) including total DOS (TDOS) and projected DOS (PDOS) is depicted in Fig. S27. High electronic states at the Fermi level for both RuSb and Ru can be observed, suggesting the metallic characteristic of both catalysts. Therefore, both RuSb and Ru could achieve high electronic conductivity [53,54], which is beneficial to improve catalytic activity. Moreover, the PDOS for RuSb in Fig. 4c and S28 suggests that the peaks of Ru 4*d* orbitals match well with that of Sb 5*p* orbitals, implying strong *p*-*d* orbital hybridization [55]. In contrast, almost no Sb 4*d* orbitals can be observed, excluding the efficient *d*-*d* interaction. Additionally, the electron localization function (ELF) in Fig. 4d indicates that the electrons are more localized around the Sb atoms, implying the existence of *p*-*d* charge transfer between Ru and Sb atoms. Meanwhile, the charge densities of RuSb and Ru are shown in Fig. 4e and Fig. S29. Obviously, the introduction of Sb atoms into Ru causes charge redistribution. The Bader charge analysis shows that an average of 0.317 |e| electrons are transferred from the Sb atom to the Ru atom in RuSb, which alters the surface electronic structure that determines the HER and HzOR activity. It is well known that water dissociation is a key RDS for alkaline and neutral HER [56]. As depicted in Fig. 4f, g, S30, and S31, the water dissociation energy barriers for RuSb (0.811 eV) and Ru (0.808 eV) are almost the same, indicating the comparable capability of RuSb and Ru in facilitating the water dissociation to form absorbed hydrogen atoms. Moreover, the hydrogen adsorption free energy (ΔG_H) of RuSb (−0.199 eV) is much close to zero than that of Ru (−0.487 eV), revealing the stronger ability of RuSb in the formation of H_2 from the absorbed hydrogen atoms (Fig. 4h and S32). Therefore, the comparable water dissociation capacity but stronger H_2 formation ability may be the reason for the better HER activity of RuSb than that of Ru in alkaline and neutral media. In addition, the ΔG_H value is decisive to the acidic HER activity of a catalyst [57,58]. Obviously, the ΔG_H value of RuSb is closer to zero in contrast with Ru, which supports the experimental result that RuSb exhibits higher HER activity than Ru in acid media. Furthermore, the thermodynamic process for HzOR on RuSb and Ru was theoretically investigated and the structural models of the reaction intermediates are shown in Fig. S33 and S34. The free energy diagrams for the HzOR process on RuSb and Ru both indicate that the dehydrogenation of

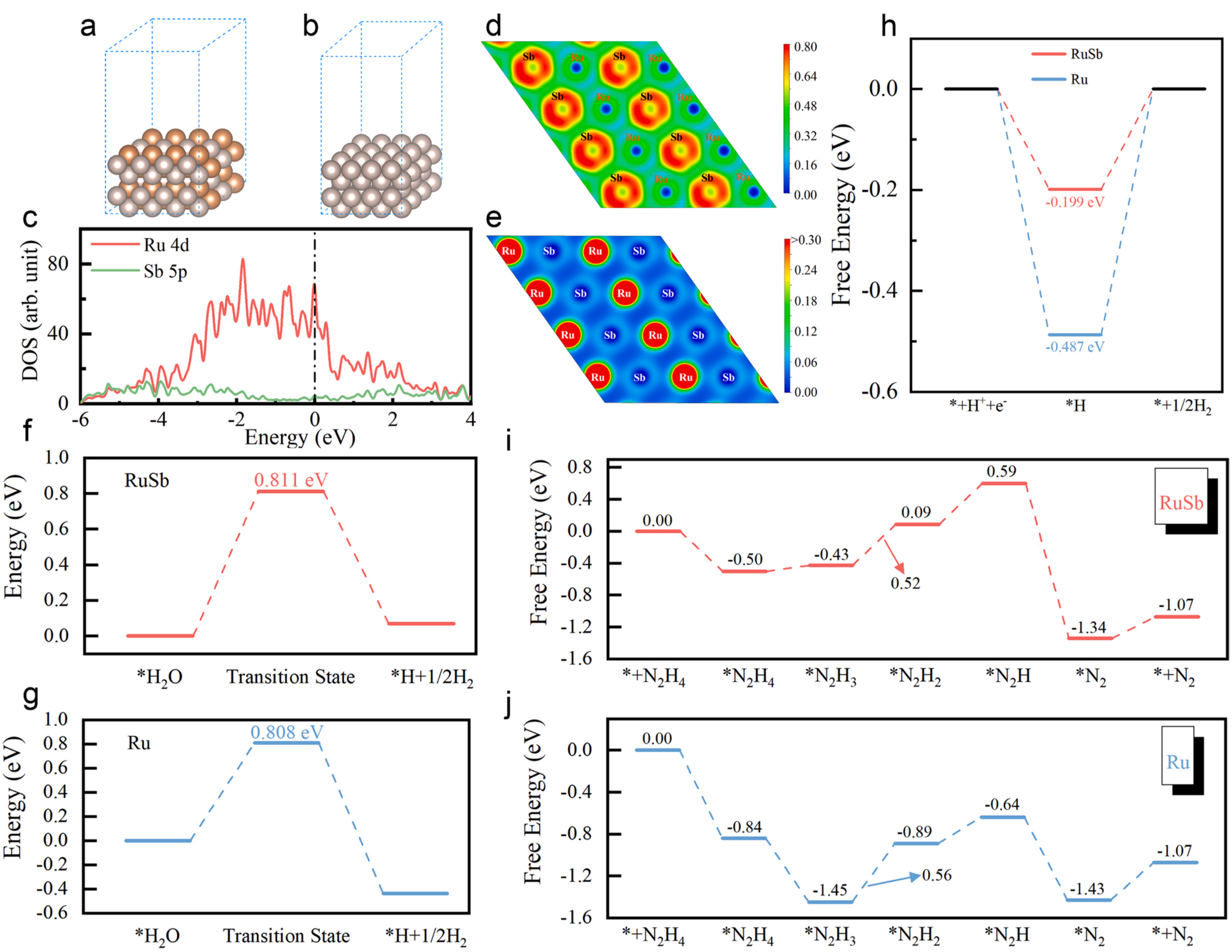

Fig. 4. Surface models of (a) RuSb and (b) Ru. The gray and brown balls represent the Ru and Sb atoms, respectively. The PDOS of Ru 4d and Sb 5p orbitals for RuSb (c). The vertical dash-dotted line represents the Fermi level. The electron localization function plot for the surface atomic layer in RuSb (d). The charge density for the surface atomic layer in RuSb. The unit is e/Bohr^3 (e). Energy diagram for water dissociation in (f) RuSb and (g) Ru. Free energy changes for HER steps in RuSb and Ru (h). Free energy changes for HzOR steps in (i) RuSb and (j) Ru.

$^*N_2H_3$ to $^*N_2H_2$ is the RDS (Fig. 4i and j). The Gibbs free energy barriers for HzOR are therefore calculated to be 0.56 and 0.52 eV in Ru and RuSb, respectively, well explaining the experimentally excellent HzOR performance for RuSb. Thus, the introduction of Sb atoms into Ru leads to strong *p-d* orbital hybridization and therefore improves the catalytic activity for both HER and HzOR.

4. Conclusion

We have established a facile hydrothermal method to fabricate RuSb nanobranches and successfully realize the regulation of both HER/HzOR activity by unique *p-d* orbital hybridization. As a result, the as-synthesized $Ru_{50}Sb_{50}$ alloy displays impressive Pt-like activity for HER, with a very low overpotential of 39 mV at 10 mA cm^{-2} in alkaline seawater. Meanwhile, $Ru_{50}Sb_{50}$ also exhibits outstanding HzOR activity with a remarkably low potential of 252 mV at 10 mA cm^{-2}. Additionally, an extraordinarily small cell voltage of 35 mV to drive 10 mA cm^{-2} in alkaline seawater was achieved for RuSb||RuSb couple, which outperforms Pt/C||Pt/C couple in the same two-electrode electrolyzer. DFT calculations reveal that Sb doping can not only make the hydrogen adsorption more thermoneutral but also decrease the energy barrier for dehydrogenation from $^*N_2H_3$ to $^*N_2H_2$. Therefore, the well-designed RuSb could provide new opportunities for the development of other bifunctional electrocatalysts in OHzS tuned by *p*-block metals or metalloids.

CRediT authorship contribution statement

Xiaofei Liu: Conceptualization, Methodology, Investigation, Data curation, Writing – original draft, Writing – review & editing. **Tianxing Wang:** Formal Analysis Investigation. **Yilin Chen:** Software, Methodology. **Jingtao Wang:** Methodology, Formal analysis Investigation. **Wenjie Xie:** Conceptualization, Methodology. **Rongqian Wu:** Writing – review & editing, Resources. **Xingtao Xu:** Methodology, Investigation. **Lihui Pang:** Formal analysis, Investigation. **Xiaogang Zhang:** Formal analysis. **Yi Lv:** Funding acquisition, Writing – review & editing, Resources. **Guangzhao Wang:** Supervision, Resources. **Yusuke Yamauchi:** Supervision, Project administration. **Tian (Leo) Jin:** Supervision, Project administration, Funding acquisition, Resources.

Declaration of Competing Interest

The authors declare that they have no known competing financial interests or personal relationships that could have appeared to influence the work reported in this paper.

Data Availability

The data that has been used is confidential.

Acknowledgements

X. Liu thanks the Fundamental Research Funds for the Central Universities (xzy012022099), Natural Science Foundation of Shaanxi Province (2023-JC-QN-0836), Institutional Foundation of The First Affiliated Hospital of Xi'an Jiaotong University (2020QN-33). T. (L.) Jin is grateful for the financial support from the National Natural Science Foundation of China (51903205), China Postdoctoral Science Foundation (2018M640970), and the Fundamental Research Funds for the Central Universities (xzy012020030). The authors gratefully acknowledge the financial support from the National Key Research and Development Project of China (Nos. 81727802 and 92048202, YL), the Key Research and Development Plan of Shaanxi Province (2022ZDLSF04-09, 2021LL-JB-06), the National Natural Science Foundation of China (No. 2020GXLH-Z-001), and the Innovation Capacity Support Plan of Shaanxi Province (No. 2020TD-040, RW). J. Wang thanks the Fundamental Research Funds for the Central Universities (2021ZYTS-24). Numerical computations were performed at Hefei Advanced Computing Center. The Instrument Analysis Center of Xi'an Jiaotong University was also acknowledged. This work was performed in part at the Queensland node of the Australian National Fabrication Facility, a company established under the National Collaborative Research Infrastructure Strategy to provide nano and microfabrication facilities for Australia's researchers.

Appendix A. Supporting information

Supplementary data associated with this article can be found in the online version at doi:10.1016/j.apcatb.2023.122771.

References

[1] Y. Li, X. Wei, L. Chen, J. Shi, Electrocatalytic hydrogen production trilogy, Angew. Chem. Int. Ed. 60 (2021) 19550–19571, https://doi.org/10.1002/anie.202009854.
[2] J. Wang, T. Liao, Z. Wei, J. Sun, J. Guo, Z. Sun, Heteroatom-doping of non-noble metal-based catalysts for electrocatalytic hydrogen evolution: an electronic structure tuning strategy, Small Methods 5 (2021), 2000988, https://doi.org/10.1002/smtd.202000988.
[3] J. Zhu, L. Hu, P. Zhao, L.Y.S. Lee, K.-Y. Wong, Recent advances in electrocatalytic hydrogen evolution using nanoparticles, Chem. Rev. 120 (2020) 851–918, https://doi.org/10.1021/acs.chemrev.9b00248.
[4] Y. Li, J. Li, Q. Qian, X. Jin, Y. Liu, Z. Li, et al., Superhydrophilic Ni-based multicomponent nanorod-confined-nanoflake array electrode achieves waste-battery-driven hydrogen evolution and hydrazine oxidation, Small 17 (2021), 2008148, https://doi.org/10.1002/smll.202008148.
[5] X. Guo, X. Wan, Q. Liu, Y. Li, W. Li, J. Shui, Phosphated IrMo bimetallic cluster for efficient hydrogen evolution reaction, eScience 2 (2022) 304–310, https://doi.org/10.1016/j.esci.2022.04.002.
[6] J. Li, C. Zhang, T. Zhang, Z. Shen, Q. Zhou, J. Pu, et al., Multiple-interface relay catalysis: Enhancing alkaline hydrogen evolution through a combination of Volmer promoter and electrical-behavior regulation, Chem. Eng. J. 397 (2020), 125457, https://doi.org/10.1016/j.cej.2020.125457.
[7] S. Shankar Naik, J. Theerthagiri, F.S. Nogueira, S.J. Lee, A. Min, G.-A. Kim, et al., Dual-cation-coordinated CoFe-layered double-hydroxide nanosheets using the pulsed laser ablation technique for efficient electrochemical water splitting: mechanistic screening by in situ/operando raman and density functional theory calculations, ACS Catal. 13 (2023) 1477–1491, https://doi.org/10.1021/acscatal.2c05017.
[8] Z. Wu, Y. Zhao, H. Wu, Y. Gao, Z. Chen, W. Jin, et al., Corrosion engineering on iron foam toward efficiently electrocatalytic overall water splitting powered by sustainable energy, Adv. Funct. Mater. 31 (2021), 2010437, https://doi.org/10.1002/adfm.202010437.
[9] Z. Lei, T. Wang, B. Zhao, W. Cai, Y. Liu, S. Jiao, et al., Recent progress in electrocatalysts for acidic water oxidation, Adv. Energy Mater. 10 (2020), 2000478, https://doi.org/10.1002/aenm.202000478.
[10] T. Jin, X. Liu, Q. Gao, H. Zhu, C. Lian, J. Wang, et al., Pyrolysis-free, facile mechanochemical strategy toward cobalt single-atom/nitrogen-doped carbon for highly efficient water splitting, Chem. Eng. J. 433 (2022), 134089, https://doi.org/10.1016/j.cej.2021.134089.
[11] J. Li, C. Zhang, H. Ma, T. Wang, Z. Guo, Y. Yang, et al., Modulating interfacial charge distribution of single atoms confined in molybdenum phosphosulfide heterostructures for high efficiency hydrogen evolution, Chem. Eng. J. 414 (2021), 128834, https://doi.org/10.1016/j.cej.2021.128834.
[12] Y. Yu, S.J. Lee, J. Theerthagiri, S. Fonseca, L.M.C. Pinto, G. Maia, et al., Reconciling of experimental and theoretical insights on the electroactive behavior of C/Ni nanoparticles with AuPt alloys for hydrogen evolution efficiency and Non-enzymatic sensor, Chem. Eng. J. 435 (2022), 134790, https://doi.org/10.1016/j.cej.2022.134790.
[13] Y. Liu, J. Zhang, Y. Li, Q. Qian, Z. Li, Y. Zhu, et al., Manipulating dehydrogenation kinetics through dual-doping Co_3N electrode enables highly efficient hydrazine oxidation assisting self-powered H_2 production, Nat. Commun. 11 (2020) 1853, https://doi.org/10.1038/s41467-020-15563-8.
[14] Q. Qian, J. Zhang, J. Li, Y. Li, X. Jin, Y. Zhu, et al., Artificial heterointerfaces achieve delicate reaction kinetics towards hydrogen evolution and hydrazine oxidation catalysis, Angew. Chem. Int. Ed. 60 (2021) 5984–5993, https://doi.org/10.1002/anie.202014362.
[15] H.-L. Huang, X. Guan, H. Li, R. Li, R. Li, S. Zeng, et al., Ir nanoclusters/porous N-doped carbon as a bifunctional electrocatalyst for hydrogen evolution and hydrazine oxidation reactions, Chem. Commun. 58 (2022) 2347–2350, https://doi.org/10.1039/D1CC06972A.
[16] T. Zhang, T. Asefa, Heteroatom-doped carbon materials for hydrazine oxidation, Adv. Mater. 31 (2019), 1804394, https://doi.org/10.1002/adma.201804394.
[17] H. Liu, Y. Liu, M. Li, X. Liu, J. Luo, Transition-metal-based electrocatalysts for hydrazine-assisted hydrogen production, Mater. Today Adv. 7 (2020), 100083, https://doi.org/10.1016/j.mtadv.2020.100083.
[18] J. Li, C. Zhang, C. Zhang, H. Ma, Y. Yang, Z. Guo, et al., Electronic configuration of single ruthenium atom immobilized in urchin-like tungsten trioxide towards hydrazine oxidation-assisted hydrogen evolution under wide pH media, Chem. Eng. J. 430 (2022), 132953, https://doi.org/10.1016/j.cej.2021.132953.

[19] J. Li, M.N. Banis, Z. Ren, K.R. Adair, K. Doyle-Davis, D.M. Meira, et al., Unveiling the nature of Pt single-atom catalyst during electrocatalytic hydrogen evolution and oxygen reduction reactions, Small 17 (2021), 2007245, https://doi.org/10.1002/smll.202007245.

[20] J. Li, J. Hu, M. Zhang, W. Gou, S. Zhang, Z. Chen, et al., A fundamental viewpoint on the hydrogen spillover phenomenon of electrocatalytic hydrogen evolution, Nat. Commun. 12 (2021) 3502, https://doi.org/10.1038/s41467-021-23750-4.

[21] A. Shan, X. Teng, Y. Zhang, P. Zhang, Y. Xu, C. Liu, et al., Interfacial electronic structure modulation of Pt-MoS_2 heterostructure for enhancing electrocatalytic hydrogen evolution reaction, Nano Energy 94 (2022), 106913, https://doi.org/10.1016/j.nanoen.2021.106913.

[22] Z. Li, W. Wang, Q. Qian, Y. Zhu, Y. Feng, Y. Zhang, et al., Magic hybrid structure as multifunctional electrocatalyst surpassing benchmark Pt/C enables practical hydrazine fuel cell integrated with energy-saving H_2 production, eScience 2 (2022) 416–427, https://doi.org/10.1016/j.esci.2022.06.004.

[23] Y. Yu, S.J. Lee, J. Theerthagiri, Y. Lee, M.Y. Choi, Architecting the AuPt alloys for hydrazine oxidation as an anolyte in fuel cell: Comparative analysis of hydrazine splitting and water splitting for energy-saving H_2 generation, Appl. Catal. B 316 (2022), 121603, https://doi.org/10.1016/j.apcatb.2022.121603.

[24] Y. Jeong, S. Shankar Naik, Y. Yu, J. Theerthagiri, S.J. Lee, P.L. Show, et al., Ligand-free monophasic CuPd alloys endow boosted reaction kinetics toward energy-efficient hydrogen fuel production paired with hydrazine oxidation, J. Mater. Sci. Technol. 143 (2023) 20–29, https://doi.org/10.1016/j.jmst.2022.09.043.

[25] S.-Y. Bae, J. Mahmood, I.-Y. Jeon, J.-B. Baek, Recent advances in ruthenium-based electrocatalysts for the hydrogen evolution reaction, Nanoscale Horiz. 5 (2020) 43–56, https://doi.org/10.1039/C9NH00485H.

[26] X. Liu, Y. Guo, W. Zhan, T. Jin, Ball milling-assisted synthesis of ultrasmall ruthenium phosphide for efficient hydrogen evolution reaction, Catalysts 9 (2019) 240, https://doi.org/10.3390/catal9030240.

[27] J. Wang, Q. Yu, H. Li, R. Li, S. Zeng, Q. Yao, et al., Natural DNA-assisted RuP_2 on highly graphitic N,P-codoped carbon for pH-wide hydrogen evolution, Chem. Commun. 57 (2021) 7284–7287, https://doi.org/10.1039/D1CC01951A.

[28] J. Li, C. Zhang, C. Zhang, H. Ma, Z. Guo, C. Zhong, et al., Green electrosynthesis of 5,5′-azotetrazolate energetic materials plus energy-efficient hydrogen production using ruthenium single-atom catalysts, Adv. Mater. 34 (2022), 2203900, https://doi.org/10.1002/adma.202203900.

[29] W. Li, Y. Liu, M. Wu, X. Feng, S.A.T. Redfern, Y. Shang, et al., Carbon-quantum-dots-loaded ruthenium nanoparticles as an efficient electrocatalyst for hydrogen production in alkaline media, Adv. Mater. 30 (2018), 1800676, https://doi.org/10.1002/adma.201800676.

[30] Q. Qian, W. Wang, G. Wang, X. He, Y. Feng, Z. Li, et al., Phase-selective synthesis of ruthenium phosphide in hybrid structure enables efficient hybrid water electrolysis under pH-universal conditions, Small 18 (2022), 2200242, https://doi.org/10.1002/smll.202200242.

[31] Y. Li, J. Zhang, Y. Liu, Q. Qian, Z. Li, Y. Zhu, et al., Partially exposed RuP_2 surface in hybrid structure endows its bifunctionality for hydrazine oxidation and hydrogen evolution catalysis, Sci. Adv. 6 (2020) eabb4197, https://doi.org/10.1126/sciadv.abb4197.

[32] J. Li, Y. Li, J. Wang, C. Zhang, H. Ma, C. Zhu, et al., Elucidating the critical role of ruthenium single atom sites in water dissociation and dehydrogenation behaviors for robust hydrazine oxidation-boosted alkaline hydrogen evolution, Adv. Funct. Mater. 32 (2022), 2109439, https://doi.org/10.1002/adfm.202109439.

[33] J. Wang, X. Guan, H. Li, S. Zeng, R. Li, Q. Yao, et al., Robust Ru-N metal-support interaction to promote self-powered H_2 production assisted by hydrazine oxidation, Nano Energy 100 (2022), 107467, https://doi.org/10.1016/j.nanoen.2022.107467.

[34] X. Guan, Q. Wu, H. Li, S. Zeng, Q. Yao, R. Li, et al., Identifying the roles of Ru single atoms and nanoclusters for energy-efficient hydrogen production assisted by electrocatalytic hydrazine oxidation, Appl. Catal. B 323 (2023), 122145, https://doi.org/10.1016/j.apcatb.2022.122145.

[35] Q. He, D. Tian, H. Jiang, D. Cao, S. Wei, D. Liu, et al., Achieving efficient alkaline hydrogen evolution reaction over a Ni_5P_4 catalyst incorporating single-atomic Ru sites, Adv. Mater. 32 (2020), 1906972, https://doi.org/10.1002/adma.201906972.

[36] X. Liu, T.L. Jin, Z.D. Hood, C. Tian, Y. Guo, W. Zhan, Mechanochemically assisted synthesis of ruthenium clusters embedded in mesoporous carbon for an efficient hydrogen evolution reaction, ChemElectroChem 6 (2019) 2719–2725, https://doi.org/10.1002/celc.201900618.

[37] T. Jin, X. Liu, Y.-Q. Su, F. Pan, X. Han, H. Zhu, et al., Mesoporous carbon-supported ultrasmall metal nanoparticles via a mechanochemical-driven redox reaction: A "Two-in-One" strategy, Appl. Catal. B 294 (2021), 120232, https://doi.org/10.1016/j.apcatb.2021.120232.

[38] T. Jin, X. Liu, H. Wang, X. Wu, Y. Zhang, Mechanochemical-assisted synthesis of ternary Ru-Ni-S pyrite analogue for enhanced hydrogen evolution performance, Carbon 162 (2020) 172–180, https://doi.org/10.1016/j.carbon.2020.02.040.

[39] B. Yang, J. Xu, D. Bin, J. Wang, J. Zhao, Y. Liu, et al., Amorphous phosphatized ruthenium-iron bimetallic nanoclusters with Pt-like activity for hydrogen evolution reaction, Appl. Catal. B 283 (2021), 119583, https://doi.org/10.1016/j.apcatb.2020.119583.

[40] F. Zhang, Y. Zhu, Y. Chen, Y. Lu, Q. Lin, L. Zhang, et al., RuCo alloy bimodal nanoparticles embedded in N-doped carbon: a superior pH-universal electrocatalyst outperforms benchmark Pt for the hydrogen evolution reaction, J. Mater. Chem. A 8 (2020) 12810–12820, https://doi.org/10.1039/D0TA04491A.

[41] Y. Liu, X. Li, Q. Zhang, W. Li, Y. Xie, H. Liu, et al., A general route to prepare low-ruthenium-content bimetallic electrocatalysts for pH-universal hydrogen evolution reaction by using carbon quantum dots, Angew. Chem. Int. Ed. 59 (2020) 1718–1726, https://doi.org/10.1002/anie.201913910.

[42] X. Wang, Y. Zhu, A. Vasileff, Y. Jiao, S. Chen, L. Song, et al., Strain effect in bimetallic electrocatalysts in the hydrogen evolution reaction, ACS Energy Lett. 3 (2018) 1198–1204, https://doi.org/10.1021/acsenergylett.8b00454.

[43] J. Wang, Y. Huang, X. Zhang, D. Cao, S. Wang, Electroless deposition of RuPd nanoparticles on porous carbon for hydrogen evolution in acid and alkaline media, Sustain. Energy Fuels 6 (2022) 2165–2169, https://doi.org/10.1039/D2SE00047D.

[44] T. Wang, X. Cao, H. Qin, L. Shang, S. Zheng, F. Fang, et al., P-block atomically dispersed antimony catalyst for highly efficient oxygen reduction reaction, Angew. Chem. Int. Ed. 60 (2021) 21237–21241, https://doi.org/10.1002/anie.202108599.

[45] B.-Q. Li, Z.-J. Xia, B. Zhang, C. Tang, H.-F. Wang, Q. Zhang, Regulating p-block metals in perovskite nanodots for efficient electrocatalytic water oxidation, Nat. Commun. 8 (2017) 934, https://doi.org/10.1038/s41467-017-01053-x.

[46] B. Hua, M. Li, W. Pang, W. Tang, S. Zhao, Z. Jin, et al., Activating p-blocking centers in perovskite for efficient water splitting, Chem 4 (2018) 2902–2916, https://doi.org/10.1016/j.chempr.2018.09.012.

[47] Z. Pu, J. Zhao, I.S. Amiinu, W. Li, M. Wang, D. He, et al., A universal synthesis strategy for P-rich noble metal diphosphide-based electrocatalysts for the hydrogen evolution reaction, Energy Environ. Sci. 12 (2019) 952–957, https://doi.org/10.1039/C9EE00197B.

[48] H. Ren, Y. Pan, C.C. Sorrell, H. Du, Assessment of electrocatalytic activity through the lens of three surface area normalization techniques, J. Mater. Chem. A 8 (2020) 3154–3159, https://doi.org/10.1039/C9TA13170A.

[49] Q. Song, X. Qiao, L. Liu, Z. Xue, C. Huang, T. Wang, Ruthenium@N-doped graphite carbon derived from carbon foam for efficient hydrogen evolution reaction, Chem. Commun. 55 (2019) 965–968, https://doi.org/10.1039/C8CC09624D.

[50] Z. Lin, B. Xiao, M. Huang, L. Yan, Z. Wang, Y. Huang, et al., Realizing negatively charged metal atoms through controllable d-electron transfer in ternary $Ir_{1-x}Rh_xSb$ intermetallic alloy for hydrogen evolution reaction, Adv. Energy Mater. 12 (2022), 2200855, https://doi.org/10.1002/aenm.202200855.

[51] Y. Zhang, G. Li, Z. Zhao, L. Han, Y. Feng, S. Liu, et al., Atomically isolated Rh sites within highly branched Rh2Sb nanostructures enhance bifunctional hydrogen electrocatalysis, Adv. Mater. 33 (2021), 2105049, https://doi.org/10.1002/adma.202105049.

[52] Z.-F. Huang, J. Song, K. Li, M. Tahir, Y.-T. Wang, L. Pan, et al., Hollow cobalt-based bimetallic sulfide polyhedra for efficient All-pH-value electrochemical and photocatalytic hydrogen evolution, J. Am. Chem. Soc. 138 (2016) 1359–1365, https://doi.org/10.1021/jacs.5b11986.

[53] B. Liu, B. He, H.Q. Peng, Y. Zhao, J. Cheng, J. Xia, et al., Unconventional nickel nitride enriched with nitrogen vacancies as a high-efficiency electrocatalyst for hydrogen evolution, Adv. Sci. 5 (2018), 1800406, https://doi.org/10.1002/advs.201800406.

[54] H. Yan, Y. Xie, Y. Jiao, A. Wu, C. Tian, X. Zhang, et al., Holey reduced graphene oxide coupled with an Mo_2N–Mo_2C heterojunction for efficient hydrogen evolution, Adv. Mater. 30 (2018), 1704156, https://doi.org/10.1002/adma.201704156.

[55] C.-J. Ruan, L.-H. Han, X. Chen, X.-C. Li, C.-F. Zhang, P.-F. Lu, et al., First principles calculations of electronic properties on $M_{13}Pt_{42}$ (M = Al, Ga, In, Mg, Ca, Sr), J. Clust. Sci. 28 (2017) 1749–1759, https://doi.org/10.1007/s10876-017-1183-3.

[56] P. Wang, X. Zhang, J. Zhang, S. Wan, S. Guo, G. Lu, et al., Precise tuning in platinum-nickel/nickel sulfide interface nanowires for synergistic hydrogen evolution catalysis, Nat. Commun. 8 (2017) 1–9, https://doi.org/10.1038/ncomms14580.

[57] H. Lv, Z. Xi, Z. Chen, S. Guo, Y. Yu, W. Zhu, et al., A new core/shell NiAu/Au nanoparticle catalyst with Pt-like activity for hydrogen evolution reaction, J. Am. Chem. Soc. 137 (2015) 5859–5862, https://doi.org/10.1021/jacs.5b01100.

[58] J.K. Nørskov, J. Rossmeisl, A. Logadottir, L. Lindqvist, J.R. Kitchin, T. Bligaard, et al., Origin of the overpotential for oxygen reduction at a fuel-cell cathode, J. Phys. Chem. B 108 (2004) 17886–17892, https://doi.org/10.1021/jp047349j.